Evaluating Coupled Climate Model Parameterizations via Skill at Reproducing the Monsoon Intraseasonal Oscillation

Patrick Orenstein*, Baylor Fox-Kemper†, Leah Johnson,

Dept. of Earth, Environmental, and Planetary Sciences (DEEPS), Brown University, Providence, RI

Qing Li,

Fluid Dynamics and Solid Mechanics, Los Alamos National Laboratory, Los Alamos, NM

and Aakash Sane

School of Engineering, Brown University, Providence, RI

*Current Affiliation: Department of Applied Physics and Applied Mathematics, Columbia University, New York, New York

†*Corresponding author address:* Baylor Fox-Kemper, DEEPS, Brown University, 324 Brook St., Providence, RI 02912

E-mail: baylor@brown.edu

ABSTRACT

Empirically generated indices are used to evaluate the skill of a global climate model in representing the monsoon intraseasonal oscillation (MISO). This work adapts the method of Suhas et al. (2013), an extended empirical orthogonal function (EEOF) analysis of daily rainfall data with the first orthogonal function indicating MISO strength and phase. This method is applied to observed rainfall and Community Earth System Model (CESM1.2) simulation results. Variants of the CESM1.2 including upper ocean parameterizations for Langmuir turbulence and submesoscale mixed layer eddy restratification are used together with the EEOF analysis to explore sensitivity of the MISO to global upper ocean process representations. The skill with which the model variants recreate the MISO strength and persistence is evaluated versus the observed MISO. While all model versions reproduce the northward rainfall propagation traditionally associated the MISO, a version including both Langmuir turbulence and submesoscale restratification parameterizations provides the most accurate simulations of the time scale of MISO events.

1. Introduction

Variability in the Indian monsoon on multiple time scales have been an area of intense research due to its significant societal and economic importance to the subcontinent and Indian Ocean periphery. Variations both year to year (interannual) and over the course of a single season (intraseasonal/subseasonal) are much harder to predict, and have been a topic of significant interest to researchers (Goswami et al. 2016; Kuppam and Mawsynram 2019). For the purposes of predictive skill, interannual and intraseasonal variability appear to be distinct phenomena, allowing—perhaps requiring—weather models to account for them separately (Krishnamurthy and Shukla 2000).

One primary mode of variability is the Indian monsoon intraseasonal oscillation (MISO), which causes brief periods of especially intense rainfall during the Asian monsoon on the Indian subcontinent and over the Bay of Bengal. At the most basic level, the MISO is defined as a deviation from the seasonal monsoon rainfall trend, which gradually increases over the course of the summer, peaks around late July, then decreases to its off-season intensity (Krishnamurti and Ardanuy 1980). This is generated in part by the annual north-south movement of the monsoonal intertropical convergence zone (Goswami and Mohan 2001). As a result, MISO events occur in an extremely complex circulation context, making them difficult to predict more than a few weeks in advance (Mo 2001). Nonetheless, they exhibit a northward propagation and some predictability, and they can be isolated using the empirical pattern recognition techniques of Suhas et al. (2013) as shown in Fig. 1. The MISO has significant marine influences and impacts, involving ocean-atmosphere heat and freshwater exchange, and is extremely dependent on the particular geometry and physical characteristics of the Bay of Bengal (Goswami et al. 2016). Li et al. (2016b, 2018) demonstrate important mixed layer-related biases in the simulations of the Bay of Bengal in the Coupled Forecast System (CFSv2), and speculate that improving mixed layer physical process representation may help. The Indian monsoon is a known source of error in CMIP5 models (Li et al. 2015).

Previous work has looked at the relationship between the interannual and intraseasonal variations in the Indian monsoon. Goswami and Mohan (2001) found that while the two behaviors act on different time scales, they are not independent phenomena. Since they exhibit similar spatial patterns, the interannual variation in monsoons can be viewed as an anomaly in intraseasonal (i.e., MISO) activity. The authors inferred that the chaotic nature of intraseasonal oscillations therefore spelled defeat for researchers trying to predict year-to-year monsoon trends. Empirical methods offer a way to circumvent this limitation by isolating modes of variation in chaotic data, and here they are extended to use in model evaluation. Through this combination of models and pattern recognition, skill in reproducing the MISO statistics can be assessed, which in turn may be used to improve forecast systems.

Not only are MISOs important to the intensity of the monsoon overall, but positive oscillation phases (indicated by red shading of the timeseries in Fig. 1 upper panel) have been shown to be correlated with a greater frequency of tropical cyclones forming in the Bay of Bengal (Akter and Tsuboki 2014). Moreover, those storms associated with a positive MISO phase tend to form at a central point in the northern Bay of Bengal and travel northwest across India, steered by the low pressure border known as the monsoon trough. The place where the storms form is a relatively small region associated with the point of greatest MISO variation in the Bay, meaning that the movement and change of the MISO over time may affect the origin and path of weather events in that region of the subcontinent (Goswami et al. 2003). A key result here is that the connectivity of rainfall over the subcontinent to the MISO variability over the Bay of Bengal is sensitive to upper ocean physics in a coupled model. Additionally, the Bay is particularly important as MISOs form in the Indian Ocean to the south and move northward, and previous studies have found a zone of peak variation to be centered on the bay (Goswami et al. 2003; Goswami and Xavier 2003; Sengupta et al. 2001).

The Community Earth System Model version 1.2 (CESM1.2: Hurrell et al. 2013) is a global coupled modeling system. The particular variants being used for this study use the standard atmosphere, sea ice, and land components, but differ in key ocean model parameterizations (Table 1). The goal in studying the MISO in these configurations was to determine if its statistics are sensitive to the upper ocean physics (as shown with less direct attribution to specific upper ocean processes in Li et al. 2016b, 2018; Samanta et al. 2018; Zhang et al. 2018), and whether optimization of these physical parameterizations might usefully improve skill in coupled forecast systems (e.g., Pattanaik et al. 2012). The specific upper ocean physical processes being evaluated are wave-induced mixing, or Langmuir turbulence, as parameterized by Li et al. (2016a) and submesoscale mixed layer eddy restratification as parameterized by Fox-Kemper et al. (2008, 2011). As of CESM1.2 the submesoscale parameterization is standard, but the Langmuir turbulence parameterization, built upon the KPP scheme (Large et al. 1994), was only included as a default setting in CESM2 (Danabasoglu et al. 2020). The CESM1.2 variants being evaluated here are prototypes including both parameterizations that preceded CESM2, but are similar in terms of the ocean model setup.

The potential importance of oceanic processes in the Bay of Bengal in setting the phasing and intensity of the MISO has been shown recently in closely related studies. Zhang et al. (2018) found a quadrature relationship between SST and precipitation in smoothed observations, indicating that these two quantities share a relationship which they presume involves warm SSTs triggering atmospheric convection. This study highlights a potential role for sea surface temperature–and the ocean mixing and restratification processes that affect it–in the phasing of monsoon active cycles. Additionally, in an atmospheric model-ocean mixed layer forecast system, the geographic distribution of mixed layer depth (held constant in time) was shown to improve forecast skill by Samanta et al. (2018), therefore processes affecting spatial distributions of mixed layer depth are likewise linked to monsoon dynamics. Therefore it is reasonable to hypothesize that processes that impact boundary layer turbulence temporally and spatially will influence monsoon variability.

Upper ocean mixing in in the Bay of Bengal is set by processes that inhibit mixing, such as buoyancy input from warming and freshwater fluxes, and those that enhance mixing such as wind driven mixing or convection. In addition to surface forcing at the air-sea interface, other processes are known to be leading order at influencing upper ocean turbulence. In particular, this work focuses on the restratifying effects of submesoscale baroclinic instability and enhanced mixing due to Langmuir circulation and turbulence, a variety of mixing that derives some of its energy from surface waves (McWilliams et al. 1997; Li et al. 2019). Submesoscale restratification plays an essential role in the upper ocean buoyancy budget where there are strong horizontal density gradients. Large freshwater input into the Bay of Bengal from river runoff (e.g., from the Bramaputra River) is stirred into the interior of the bay and creates sharp buoyancy fronts and filaments (MacKinnon et al. 2016; Ramachandran et al. 2018; Spiro Jaeger and Mahadevan 2018; Sarkar et al. 2016). Instabilities that occur at submesoscale fronts act to slump horizontal buoyancy gradients to create vertical stratification and inhibit upper ocean mixing (Boccaletti et al. 2007; Fox-Kemper et al. 2008). Conversely, Langmuir turbulence results from wind-wave interaction which creates parallel rotating cells $\sim 10^1$ m deep and is known to enhance turbulence in the ocean surface boundary layer (Langmuir 1938; Leibovich 1983; McWilliams et al. 1997; McWilliams and Sullivan 2000; Li et al. 2019). The shoaling/deepening effects of these processes have been parameterized for coarse-resolution models such as global circulation models and coupled weather forecast models that cannot simulate these processes directly.

Previous studies have defined MISOs using a variety of indices, including atmospheric vorticity at 850 hPa (Goswami et al. 2003), zonal wind (Goswami and Mohan 2001), and sea surface temperature at a stationary buoy (Sengupta et al. 2001). These choices reflected authors' assumptions about MISO dynamics; for instance, Goswami and Mohan (2001)'s use of zonal wind in the Bay of Bengal as a metric reflected their view that MISOs were an expression of breaks in the prevailing monsoon winds.

The methodology presented here is different in two ways. First, it uses rainfall data, meaning MISOs are measured by their effects, not their causes, insulating the analysis from discussions of the mechanisms of individual MISO phases. While increased rainfall alone does not define a MISO, it is a well-established relationship (and the most impactful on human activity). Second, this work expands on the technique of Suhas et al. (2013), using an extended empirical orthogonal function (EEOF) analysis to identify the oscillatory signal of the MISO rainfall data. Empirical orthogonal function (EOF) analysis decomposes complex data sets into their primary modes of variability, revealing which geographic and temporal patterns are most significant to the overall variability (Thomson and Emery 2001). This allows spatially-stationary oscillatory patterns (e.g., standing waves) to be revealed (Fox-Kemper 2004). Extended empirical orthogonal function (EEOF) analysis takes this a step further, using in this case multiple snapshots over a short time window as the "pattern" being recognized constructed to reveal propagating modes of variability (Eshel 2012; Weare and Nasstrom 1982). The EEOFs tend to isolate the northward propagation characteristic of the classical MISO phase progression (Suhas et al. 2013).

This work will use an EEOF methodology to isolate MISO events and compare different formulations of upper ocean parameterizations within CESM with observations. The comparison provides insight into how much of a difference upper ocean processes have on MISO events, as well as more generally how well the CESM1.2 simulates the MISO. CESM is a climate rather than a weather forecast model, so the issue of model skill is focused on the model's ability to simulate a realistic MISO with reasonable magnitude and recurrence, rather than its ability to produce good forecasts from observed initial conditions. However, as the National Center for Environmental Predictions (NCEP) Coupled Forecast System (CFS) is often used in this region shares significant code and capabilities with the CESM, implications for what constitutes a skillful CESM is expected to resemble what constitutes a skillful CFS.

2. Methods

a. Observational Data

Following Suhas et al. (2013), the observational data set used for model comparison is the Global Precipitation Climatology Project (GPCP), a reanalysis based on both satellite and historical observations (Huffman et al. 1997; Adler et al. 2003; Huffman et al. 2009). This data set in 1×1 degree resolution was obtained for Oct. 1, 1996 to Sept. 30, 2015. This data was regridded onto the 1.9×2.5 grid of the CESM atmospheric model for comparison.

b. CESM

This work uses the the National Center for Atmospheric Research (NCAR) Community Earth System Model, version 1.2 (CESM1.2). Previously, CESMv1 was found to have the smallest bias in simulating the monsoon compared to other CMIP5 models (Anand et al. 2018). The model configuration includes a fully coupled atmosphere (CAM4) and land (CLM4.0) on a 1.9×2.5 degree nominal grid, and ocean (POP2) along with sea-ice (CICE4) on the $gx1$ version 6 grid (1 degree nominal resolution), and waves (WAVEWATCH III v3.14) on a coarser grid (Li et al. 2016a). The model is run for 100 years with steady preindustrial conditions. This analysis uses the last 30 years of integration after which the model is assumed to be sufficiently equilibrated in the upper ocean, as mixed layer depths are stable when different decades at the end of the simulation are compared. Boundary layer turbulence is parameterized using the K-profile parameterization (KPP) mixing scheme (Large et al. 1994), and the additional effects of restratification by submesoscale mixed layer eddies (Fox-Kemper et al. 2011) and enhanced vertical mixing through Langmuir turbulence (Li et al. 2016a) can be switched on or off. The different simulations for comparison are all forced with the same conditions and from the same initial conditions, they differ only in this aspect (Table 1).

The effects of submesoscale baroclinic instability is parameterized as an overturning streamfunction (Fox-Kemper et al. 2008, 2011),

$$\Psi_o = \frac{\Delta s}{L_f} C_e \frac{H^2 \nabla_h b \times \widehat{\mathbf{z}}}{|f|} \mu(z) \tag{1}$$

$$\mu(z) = \left[1 - \left(\frac{2z}{H} + 1\right)^2\right]\left[1 + \frac{5}{21}\left(\frac{2z}{H} + 1\right)^2\right] \tag{2}$$

Where C_e is a constant set to 0.06, H is mixed layer depth as determined by a density difference from the surface, b is the buoyancy formed from the density ρ and background density ρ_0 by $b = g(\rho_0 - \rho)/\rho_0$, $\nabla_h b$ is the grid scale horizontal buoyancy gradient and the factor $\Delta s/L_f$ includes the horizontal grid scale and a frontal scaling factor that accounts for the course horizontal resolution of the model (Fox-Kemper et al. 2011). The typical effect of this parameterization is to shoal the mixed layer by overturning lateral fronts wherever they are present to increase the vertical stratification, at a rate consistent with simulations and observations of mixed layer eddy processes.

The Langmuir turbulence parameterization developed by Li et al. (2016a) accounts for the additional vertical boundary layer mixing that occurs when Stokes drift from surface waves (which is extracted from the WaveWatch III component model across the globe and depends on the winds and ocean currents of the other model components) interacts with near-surface boundary layer turbulence resulting in downward accelerations by a wave-current interaction called the Stokes shear force (Suzuki and Fox-Kemper 2016). The rate of additional mixing beyond wind-driven mixing is estimated in Large Eddy Simulations resolving Langmuir turbulence (Van Roekel et al. 2012) and included in KPP following the parameterization form suggested by McWilliams and Sullivan (2000). The parameterization mostly increases the vertical turbulent velocity scale within the boundary layer by an enhancment factor $\mathscr{E}$:

$$W = \frac{ku^*}{\phi} \to W = \frac{ku^*}{\phi}\mathscr{E}, \tag{3}$$

$$\mathscr{E} = |\cos\alpha|\sqrt{1+(c_1 La)^{-2}+(c_2 La)^{-4}} \tag{4}$$

The angle α is the predicted angle between the Langmuir cell orientation and the surface wind orientation, $c_1 = 1.5, c_2 = 5.4$ are dimensionless constants, and La is the surface layer-averaged, turbulent Langmuir number formed from projecting both the wind stress and Stokes drift into the Langmuir cell orientation (Van Roekel et al. 2012; Li et al. 2016a), or

$$La = \sqrt{\frac{u^* \cos\alpha}{|\langle u_s \rangle| \cos(\theta_{ww} - \alpha)}} \tag{5}$$

Here θ_{ww} is the angle between the wind and the wave direction, $\langle u_s \rangle$ is the Stokes drift averaged over the surface layer –i.e., the upper 20% of the mixed layer (Harcourt and DAsaro 2008)–and α is found from application of the Law of the Wall as derived in Van Roekel et al. (2012). The additional effects of Langmuir mixing on entrainment at the mixed layer base (Li and Fox-Kemper 2017) were not used for this study.

In summary, the submesoscale restratification depends on the horizontal buoyancy gradient and mixed layer depth and acts to shoal the ML. Conversely, Langmuir turbulence depends on waves and wind direction and strength, and acts to deepen the mixed layer. The combinations of parameterizations and cases are outlined in Table 1. These parameterizations rely on different resolved variables and therefore have different temporal and geographical influences over the Bay of Bengal and globally. It should be noted that both of these parameterizations are the default in CESM2

(Danabasoglu et al. 2020), so the sensitivity under study is the effect of turning each of or both of them off.

Each model with its own parameterization set was initialized identically for 30-year runs. For analysis of the MISO, the annual mean and first three harmonics of the precipitation fields were removed, so that only sub-seasonal precipitation anomaly variations were retained. Then, a zonal average of precipitation data between 12.5S–30.5N and 60.5–95.5E isolated the region of interest. This choice has the advantage of eliminating any topography from the analysis region.

c. EEOF Analysis

Empirical orthogonal functions (EOFs) are an application of singular value decomposition (SVD) which treats the decomposed values as representations of the temporal and spatial variability of a data set (Thomson and Emery 2001). The following equation shows the archetypal SVD in matrix notation,

$$\mathbf{M} = \mathbf{U}\mathbf{S}\mathbf{V}^{T} \tag{6}$$

where $\mathbf{M}$ is a spatiotemporal data set organized with rows and columns as spatial grid locations and time steps, $\mathbf{U}$ and $\mathbf{V}$ are its left and right singular vectors, and $\mathbf{S}$ is the matrix of singular values. $\mathbf{V}$ is a square matrix with the same dimensions as the spatial grid of the original data matrix and each of its columns is a normalized pattern or mode of spatial variability that repeats in the anomaly data. The different patterns are guaranteed to be orthogonal. The left matrix $\mathbf{U}$ is a square matrix the size of the number of time steps in the data matrix, and each of its columns captures the normalized time series of each corresponding spatial mode, respectively. The time series are also orthogonal. $\mathbf{S}$ is a diagonal matrix capturing the amplitude and relative importance of each mode, typically ordered from the largest amplitude to the smallest. Note that orthonormality of $\mathbf{U}$ and $\mathbf{V}$ implies that the sum of the diagonals of $\mathbf{S}^2$ equals that of the original data matrix times its transpose, indicating that the spatiotemporal variance explained by each mode is captured by the corresponding singular value squared. The fraction of the variance represented by a particular mode is captured by the corresponding diagonal element squared divided by the sum of the squares of all of the diagonal elements of S. Similarly, (6) implies that the original data can be reconstructed from U,S,V, or approximated by retaining only a limited number of modes with the largest entry on the diagonal of S.

A temporal extended EOF (EEOF) involves expanding the original M matrix by concatenating a duplicate of the data set which is offset (or "lagged") in time. Thus, the lagged data follows the same form as (6) has for a dataset with more spatial grid points. By simultaneously performing EOF analysis on the same data from slightly different starting times, a mode in a temporal EEOF captures not a single spatial pattern, but a sequential pattern of two consecutive days of evolving features (Weare and Nasstrom 1982). Here, an EEOF with lags ranging from 1-16 days (17 total days) is used to recognize patterns in the short-term evolution of the precipitation–i.e., the range of time expected for the MISO development. Terminology for EOFs and EEOFs varies widely:extended empirical orthogonal functions with a number indicating their relative importance in terms of the corresponding S entry (e.g., EEOF1, EEOF2) and the time series describing the evolving amplitude of each set of lagged patterns are called principal components again numbered by importance (e.g. PC1, PC2). If the S values are all distinct, then each EEOF and PC are unique and distinct.

EOF analysis in general is purely statistical and lacks dynamical cause-and-effect (Dommenget and Latif 2002), so the decomposed modes may not have any physical significance unless independently shown to do so. EOFs may produce apparent order in data beyond what is present. EOF analysis is particularly troubling if the real modes of variability are not orthogonal in time or space. EOF analysis can also be confusing when representing propagating patterns (Fox-Kemper

2004), but the EEOF approach makes rapidly propagating patterns simple to describe with a single EEOF. In this case, the MISO is well understood to be a north-south phenomenon, making it more natural to apply an EEOF method than in the case of, for instance, a spatial data set with no a priori assumptions about modes of variability. The method is not being used here to identify unseen patterns but to evaluate one already identified.

As shown by Suhas et al. (2013) the EEOFs produced in this manner agree with other indices of MISO variability. Fig. 1 shows the variation in PC1 over a few positive and negative phases of EEOF1, and the corresponding zonal-mean precipitation over the region below. It is clear that the northward-propagating precipitation pattern is captured by the PC1 time series, and the EEOF spatial pattern of propagation similarly matches the precipitation propagation (not shown). Following Suhas et al. (2013), EEOF1 and EEOF2 are normalized by their standard deviations, and are hereafter referred to as MISO1 and MISO2. For the purposes of this work, MISO maxima and minima are identified here as peaks and troughs in MISO1 (delineated by the 5th and 95th percentiles over the whole record). Other EOF-based definitions are common, e.g., for evaluating the Madden-Julian Oscillation (such as Kim and North 1999) or other climate variability signals (Weiss et al. 2019). In this case, MISO1 isolates the primary north-south mode of oscillation.

The meaning of the PCA1 appears clearly by plotting MISO1 alongside zonal precipitation (Figure 1). The precipitation data show clear northward-moving phenomena associated with peaks and valleys in PC1.

d. Composite Maps

Composite maps of the difference in regional rainfall anomaly between active and break phases of the MISO are a complementary metric to the MISO1 pattern once the maximum and minimum MISO stages are found (Fig. 2). While the EEOF is formulated based only on rainfall in the Bay of Bengal, composite plots of these time periods show a wider region, illustrating how the MISO phases defined by the EEOF manifest in the Indian Ocean as a whole. Furthermore, the composite precipitation averages are not limited by orthogonality of spatial patterns, or the fact that the linear construction of the EEOFs ensures symmetries that may not be present: e.g., EEOF1 in a positive phase is exactly the same as the negative of EEOF1 in a negative phase. Fig. 3 illustrates that the composites over positive and negative phases indeed differ in spatial pattern.

3. Results and Discussion

Solely matching the timescale of simulated MISO phenomenon identified by the EEOF analysis to that previously observed for the MISO does not indicate a complete model success, but together with a good spatial structure of the EEOFs and the patterns of the composite maps (Figure 2) alternative mechanisms become increasingly unlikely. The short lag interval (1-16 days) chosen for EEOF-based MISO detection is insufficient to cover a full repetition of a MISO event followed by another, but it does capture the characteristic northward trend of the precipitation maximum within an individual event (Figure 1).

The composite maps (Figure 2) of the difference in precipitation anomaly between MISO positive and negative phase peaks (MISO1 maxima and minima) show clear regions of strong variability throughout the Bay of Bengal and the surrounding region. The GPCP data has a strong positive center stretching from the Bay of Bengal across India to the Arabian Sea. Closer to the equator, there is a diffuse precipitation minimum during the MISO positive phase. These precipitation patterns are not an input to the detection algorithm for EEOF1, but are consistently correlated with it. The models do a fair job of capturing the Bay of Bengal center of activity, but tend to either overestimate the precipitation anomaly over Indonesia or underestimate the precipitation anomaly over western India. None of them show a positive anomaly region stretching as far west as in the GPCP data. Conversely, in all of the models, the opposing precipitation anomaly near the equator is too strong compared to the observations. Overall, the CESM control run including both Langmuir and mixed layer eddy parameterizations tends to have the closest pattern to the GPCP observations.

The EEOFs for all of the data sets have very broad singular value distributions, meaning the first few EEOFs account for only a modest portion of the variance which captures many other sources of precipitation variability. In GPCP, the first two EEOFs explain 9.80% and 8.97% of the total variance respectively. For the CESM control run with both Langmuir and submesoscale turbulence, the first two EEOFs explain 7.83% and 6.87% of the variance. Removing Langmuir turbulence leaves 7.73% and 6.24%, while removing submesoscale turbulence gives a greater spread of 7.86% and 6.03%. Removing both gives 8.01% and 6.89% (Figure 4). Thus, the MISO is stronger as a fraction of total precipitation variance in the real world than in the simulations, which tend to spread precipitation variance more evenly among modes. In absolute terms, the first 2 singular values for all CESM versions are weaker than those for GPCP data, consistent with the MISO1 index accounting for more of the variation in the observations than in the model runs.

Active, or positive, MISO period identified in observations by the EEOF method have an average period of 31 days (Figure 5 top row), which is consistent with previous descriptions of the MISO as approximately 30-60 days long (Goswami et al. 2016). This recurrence time exceeds the lag interval used to formulate the EEOF. The control model version exhibits the most similar behavior, with active periods on average 37 days long. The two model versions without Langmuir turbulence show the greatest difference difference from the observations: the noLT version has active phases on average 52 days long, while the noLTSM version has 123 days. This trend is similarly evident in the distribution of negative MISO phases (right column). Note the difference in sample size caused by the longer time span of the model runs.

Figure 6 shows that while the CESM simulations including parameterizations of mixed layer eddies and Langmuir turbulence do have the most similar MISO statistics to the GPCP, the mixed layer depth in the Bay of Bengal, and the north-south gradient of mixed layer depth differ significantly from an observations for this simulation, here drawn from the Monthly Isopycnal Mixed Layer Climatology (MIMOC, Schmidtko et al. (2013)). The definition of mixed layer used in the CESM and in MIMOC is consistent, so the distinctions are not semantic. MIMOC has shallower mixed layer depths, and less seasonal variation in mixed layer depth than CESM. Furthermore, the simulation that performs best in the MISO (mixed layer eddies and Langmuir mixing: yellow line) does *not* have the mixed layer depth closest to observations. This comparison of mixed layer depths indicates that 1) the CESM can still be improved, and 2) under the coarse vertical resolution and numerics of the CESM a "good" mixed layer depth may not select for the best MISO variability, and 3) there are likely other model biases (e.g., clouds, precipitation, or atmospheric boundary layer parameterizations) that are providing additional errors beyond those being assessed here by altering the upper ocean parameterizations. Alternatively, it is possible that it is changes to the mixed layer *outside* of the Bay of Bengal that are having a beneficial effect on dynamics within the bay–an issue that cannot be addressed with the global model design used here. Thus, a variety of diagnostics, such as the method of Suhas et al. (2013) chosen here, are needed to fully assess the MISO and models' ability to predict it.

4. Conclusions

The EEOF method of Suhas et al. (2013) captures local modes of variability like the MISO. In this analysis, the MISO statistics are significantly sensitive to upper ocean parameterizations, here Langmuir turbulence and mixed layer eddy parameterizations, even when all other aspects of the model are unchanged. Thus, upper ocean physics nontrivially impacts the MISO.

The upper ocean turbulence plays a large role in ocean-atmosphere interactions and the MISO is an inherently marine weather phenomena. However, most numerical weather prediction system analyses tend to focus on simulation of sea surface temperature, not mixed layer depth. The models here differ in both SST anomaly statistics and mixed layer depth, but these are not easily separated as both effects stem from substituting among self-consistent parameterizations. If solely the SST warming of submesoscale restratification was included without altering the mixed layer depth, it would not be physically meaningful.

The composite maps shown for CESM (Figure 2) show that it is not only persistence of the MISO phenomena that is affected by upper ocean physics, but also the spatial patterns can be made more or less realistic. The effects near the equator, where all of the simulations have too little coherent precipitation with the positive MISO phase, indicates that there are likely other biases to address, e.g., the double ITCZ bias (Zhang et al. 2019).

Interestingly, the Bay of Bengal mixed layer depths of the model most successful in simulating the MISO are not the most accurate in comparison to observations. Thus, the mechanisms at play in the model to simulate the MISO are different than those in the real world–a fact that is not surprising given the complexity of the cloud formations in a real MISO (Kumar et al. 2017) versus the simplified MISO in the CESM. It is not at all clear if the model improvements shown here are a vindication of the particular set of parameterizations chosen, or just a coincidental set of factors combining into an improved MISO.

What is clear however, is that the simulated MISO is sensitive to upper ocean physics that contributes to mixed layer balances, not just prescribed mixed layer depths (Samanta et al. 2018). Furthermore, in this particular model, the most realistic MISO did not occur in the model with the most accurate mixed layer depth, revealing that the whole of the model, including other inaccuracies, need to be taken into account when assessing forecast skill potential.

Methods like EEOF analysis can help identify such phenomena and define a rigorous way to extract targeted skill tests from observations and climate models in such a way that they can be directly compared. Measuring precipitation alone without the added perspective of the EEOF framework significantly decreases the clarity of the connection between the upper ocean physics and the MISO, since upper ocean physics also affects other aspects of the precipitation patterns that conceal the MISO impact. On the other hand, EEOFs hold the potential to indicate modes of oscillation where there may be none, so patterns and temporal progression and persistence need to be evaluated as done here.

EOFs (and EEOFs) can also provide the basis for an empirical prediction system (Penland and Magorian 1993; Weiss et al. 2019) which can offer comparable forecast skill to full process-based modeling systems (Newman and Sardeshmukh 2017). Thus, the results here that upper ocean processes affect MISO EEOF statistics is likely to impart an impact on the potential forecast skill of process-based models.

The independence of EEOF analysis from model physics is both a strength and a weakness of the methodology. On the one hand, by making no assumptions about the dynamics of MISO events an EEOF can focus purely on their observed empirical behavior. Additionally, here we compound this agnosticism by using precipitation as our base variable, focusing on an effect of a MISO rather than a theorized mechanism. However, a more detailed look into the changing coupled air-sea mechanisms triggered by the different upper ocean physics is an important next step to better understand the nature of the sensitivity found here.

Comparing versions of a GCM with and without various forms of turbulence has significant value from the perspective of climate mechanisms and model physics. Since the precipitation patterns associated with MISOs form in the Indian Ocean and move North through the Bay of Bengal, this model comparison provides an opportunity to test how important ocean turbulence is to such synoptic scale phenomena. However, as the perturbed physics in this CESM ensemble was perturbed *globally*, it is not clear if the local effects on the upper Bay of Bengal was the key change, or if other regions affected the initiation of the MISOs elsewhere, for example. The mismatch between model MISO accuracy and Bay of Bengal mixed layer depths would be natural if the improved skill descended from changes elsewhere rather than local changes. Using perturbed Bay of Bengal physics in a regional climate model forced with identical remote forcing can distinguish between the impacts of local and remote physics, as can better understanding of the perturbed mechanisms underlying these changes to the MISO.

The importance of intraseasonal behavior to global climate predictions has become clear over the last decade. The most significant mode of East-West tropical intraseasonal variation, the Madden-Julian oscillation (MJO), has been shown in GCMs to nearly double in simulations with quadrupled atmospheric CO_2 levels. The precipitation anomalies associated with the MJO are projected to increase by 10% with every degree C of surface temperature warming, partly due to increases in surface heat flux, but primarily due to a significant increase in vertical atmospheric circulation (Arnold et al. 2015). Since MISOs exhibit a similar mechanism, their response to climate change should be studied once a climate model is vetted for adequacy.

Acknowledgments. BFK, LJ, and AS funded by ONR N00014-17-1-2393. Computing supported by NSF 1655221. Conversations with Eric D'Asaro, Amit Tandon, Jen MacKinnon, and others on the MISO-BoB team helped to focus this work. The Global Precipitation Climatology Project (GPCP) 1 Degree Daily product may be obtained at https://www.ncdc.noaa.gov/wdcmet/data-access-search-viewer-tools/global-precipitation-climatology-project-gpcp-clearinghouse. All CESM data used here are available on the Brown University digital repository (https://repository.library.brown.edu). The Monthly

Isopycnal Mixed Layer Climatology (MIMOC, Schmidtko et al. (2013)) may be accessed at http://www.pmel.noaa.gov/mimoc/.

References

Adler, R. F., and Coauthors, 2003: The Version-2 Global Precipitation Climatology Project (GPCP) Monthly Precipitation Analysis (1979Present). *J. Hydrometeor.*, **4 (6)**, 1147–1167, doi:10.1175/1525-7541(2003)004⟨1147:TVGPCP⟩2.0.CO;2, URL https://journals.ametsoc.org/doi/abs/10.1175/1525-7541(2003)004%3C1147:TVGPCP%3E2.0.CO;2.

Akter, N., and K. Tsuboki, 2014: Role of synoptic-scale forcing in cyclogenesis over the bay of bengal. *Climate dynamics*, **43 (9-10)**, 2651–2662.

Anand, A., S. K. Mishra, S. Sahany, M. Bhowmick, J. S. Rawat, and S. K. Dash, 2018: Indian Summer Monsoon Simulations: Usefulness of Increasing Horizontal Resolution, Manual Tuning, and Semi-Automatic Tuning in Reducing Present-Day Model Biases. *Scientific Reports*, **8 (1)**, 3522, doi:10.1038/s41598-018-21865-1, URL https://www.nature.com/articles/s41598-018-21865-1.

Arnold, N. P., M. Branson, Z. Kuang, D. A. Randall, and E. Tziperman, 2015: MJO Intensification with Warming in the Superparameterized CESM. *J. Climate*, **28 (7)**, 2706–2724, doi:10.1175/JCLI-D-14-00494.1, URL https://journals.ametsoc.org/doi/abs/10.1175/JCLI-D-14-00494.1.

Boccaletti, G., R. Ferrari, and B. Fox-Kemper, 2007: Mixed Layer Instabilities and Restratification. *Journal of Physical Oceanography*, **37 (9)**, 2228–2250, doi:10.1175/JPO3101.1, URL https://doi.org/10.1175/JPO3101.1http://journals.ametsoc.org/doi/abs/10.1175/JPO3101.1.

Danabasoglu, G., and Coauthors, 2020: The community earth system model version 2 (cesm2). *Journal of Advances in Modeling Earth Systems*, **12 (2)**, e2019MS001 916.

Dommenget, D., and M. Latif, 2002: A Cautionary Note on the Interpretation of EOFs. *J. Climate*, **15 (2)**, 216–225, doi:10.1175/1520-0442(2002)015⟨0216:ACNOTI⟩2.0.CO;2, URL https://journals.ametsoc.org/doi/abs/10.1175/1520-0442(2002)015%3C0216:ACNOTI%3E2.0.CO%3B2.

Eshel, G., 2012: *Spatiotemporal Data Analysis*. Princeton University Press.

Fox-Kemper, B., 2004: Wind-driven barotropic gyre II: Effects of eddies and low interior viscosity. *J. Mar. Res.*, **62**, 195–232, doi:info:doi/10.1357/0022240047774201690, URL https://www.ingentaconnect.com/content/jmr/jmr/2004/00000062/00000002/art00003.

Fox-Kemper, B., R. Ferrari, and R. Hallberg, 2008: Parameterization of Mixed Layer Eddies. Part I: Theory and Diagnosis. *J. Phys. Oceanogr.*, **38 (6)**, 1145–1165, doi:10.1175/2007JPO3792.1, URL https://journals.ametsoc.org/doi/full/10.1175/2007JPO3792.1.

Fox-Kemper, B., and Coauthors, 2011: Parameterization of mixed layer eddies. III: Implementation and impact in global ocean climate simulations. *Ocean Modelling*, **39 (1)**, 61–78, doi:10.1016/j.ocemod.2010.09.002, URL http://www.sciencedirect.com/science/article/pii/S1463500310001290.

Goswami, B., S. A. Rao, D. Sengupta, and S. Chakravorty, 2016: Monsoons to Mixing in the Bay of Bengal: Multiscale Air-Sea Interactions and Monsoon Predictability. *Oceanography*, **29 (2)**, 18–27, URL https://www.jstor.org/stable/24862666.

Goswami, B. N., R. S. Ajayamohan, P. K. Xavier, and D. Sengupta, 2003: Clustering of synoptic activity by Indian summer monsoon intraseasonal oscillations. *Geophys. Res. Lett.*, **30 (8)**, 1431, doi:10.1029/2002GL016734, URL http://onlinelibrary.wiley.com/doi/10.1029/2002GL016734/abstract.

Goswami, B. N., and R. S. A. Mohan, 2001: Intraseasonal Oscillations and Interannual Variability of the Indian Summer Monsoon. *J. Climate*, **14 (6)**, 1180–1198, doi:10.1175/1520-0442(2001)014⟨1180:IOAIVO⟩2.0.CO;2, URL http://journals.ametsoc.org/doi/abs/10.1175/1520-0442(2001)014%3C1180:IOAIVO%3E2.0.CO;2.

Goswami, B. N., and P. K. Xavier, 2003: Potential predictability and extended range prediction of Indian summer monsoon breaks. *Geophysical Research Letters*, **30 (18)**, doi:10.1029/2003GL017810, URL https://agupubs.onlinelibrary.wiley.com/doi/abs/10.1029/2003GL017810.

Harcourt, R. R., and E. A. DAsaro, 2008: Large-eddy simulation of Langmuir turbulence in pure wind seas. *Journal of Physical Oceanography*, **38 (7)**, 1542–1562.

Huffman, G. J., R. F. Adler, D. T. Bolvin, and G. Gu, 2009: Improving the global precipitation record: GPCP Version 2.1. *Geophysical Research Letters*, **36 (17)**, doi:10.1029/2009GL040000, URL https://agupubs.onlinelibrary.wiley.com/doi/abs/10.1029/2009GL040000.

Huffman, G. J., and Coauthors, 1997: The Global Precipitation Climatology Project (GPCP) Combined Precipitation Dataset. *Bull. Amer. Meteor. Soc.*, **78 (1)**, 5–20, doi:10.1175/1520-0477(1997)078⟨0005:TGPCPG⟩2.0.CO;2, URL https://journals.ametsoc.org/doi/abs/10.1175/1520-0477(1997)078%3C0005:TGPCPG%3E2.0.CO;2.

Hurrell, J. W., and Coauthors, 2013: The community earth system model: a framework for collaborative research. *Bulletin of the American Meteorological Society*, **94 (9)**, 1339–1360.

Kim, K.-Y., and G. R. North, 1999: EOF-Based Linear Prediction Algorithm: Examples. *J. Climate*, **12 (7)**, 2076–2092, doi:10.1175/1520-0442(1999)012⟨2076:EBLPAE⟩2.0.CO;

2, URL https://journals.ametsoc.org/doi/full/10.1175/1520-0442%281999%29012%3C2076%3AEBLPAE%3E2.0.CO%3B2.

Krishnamurthy, V., and J. Shukla, 2000: Intraseasonal and Interannual Variability of Rainfall over India. *J. Climate*, **13 (24)**, 4366–4377, doi:10.1175/1520-0442(2000)013⟨0001:IAIVOR⟩2.0.CO;2, URL https://journals.ametsoc.org/doi/abs/10.1175/1520-0442(2000)013%3C0001:IAIVOR%3E2.0.CO%3B2.

Krishnamurti, T. N., and P. Ardanuy, 1980: The 10 to 20-day westward propagating mode and Breaks in the Monsoons. *Tellus*, **32 (1)**, 15–26, doi:10.1111/j.2153-3490.1980.tb01717.x, URL https://onlinelibrary.wiley.com/doi/abs/10.1111/j.2153-3490.1980.tb01717.x.

Kumar, S., A. Arora, R. Chattopadhyay, A. Hazra, S. A. Rao, and B. Goswami, 2017: Seminal role of stratiform clouds in large-scale aggregation of tropical rain in boreal summer monsoon intraseasonal oscillations. *Climate Dynamics*, **48 (3-4)**, 999–1015.

Kuppam, A. P., and M. Mawsynram, 2019: The South Asian monsoon, past, present and future. *The Economist*, URL https://www.economist.com/essay/2019/06/27/the-south-asian-monsoon-past-present-and-future.

Langmuir, I., 1938: Surface Motion of Water Induced by Wind. *Science*, **87 (2250)**, 119–123, URL https://www.jstor.org/stable/1664575.

Large, W. G., J. C. McWilliams, and S. C. Doney, 1994: Oceanic vertical mixing: A review and a model with a nonlocal boundary layer parameterization. *Reviews of Geophysics*, **32 (4)**, 363–403, doi:10.1029/94RG01872, URL https://agupubs.onlinelibrary.wiley.com/doi/abs/10.1029/94RG01872.

Leibovich, S., 1983: The Form and Dynamics of Langmuir Circulations. *Annual Review of Fluid Mechanics*, **15 (1)**, 391–427, doi:10.1146/annurev.fl.15.010183.002135, URL https://doi.org/10.1146/annurev.fl.15.010183.002135.

Li, G., S.-P. Xie, and Y. Du, 2015: Monsoon-Induced Biases of Climate Models over the Tropical Indian Ocean. *J. Climate*, **28 (8)**, 3058–3072, doi:10.1175/JCLI-D-14-00740.1, URL https://journals.ametsoc.org/doi/full/10.1175/JCLI-D-14-00740.1.

Li, Q., and B. Fox-Kemper, 2017: Assessing the effects of langmuir turbulence on the entrainment buoyancy flux in the ocean surface boundary layer. *Journal of Physical Oceanography*, **47 (12)**, 2863–2886.

Li, Q., A. Webb, B. Fox-Kemper, A. Craig, G. Danabasoglu, W. G. Large, and M. Vertenstein, 2016a: Langmuir mixing effects on global climate: WAVEWATCH III in CESM. *Ocean Modelling*, **103**, 145–160, doi:10.1016/j.ocemod.2015.07.020, URL http://www.sciencedirect.com/science/article/pii/S1463500315001407.

Li, Q., and Coauthors, 2019: Comparing ocean boundary vertical mixing schemes including Langmuir turbulence. *Journal of Advances in Modeling Earth Systems (JAMES)*, doi:10.1029/2019MS001810, URL https://doi.org/10.1029/2019MS001810.

Li, Y., W. Han, W. Wang, and M. Ravichandran, 2016b: Intraseasonal variability of sst and precipitation in the arabian sea during the indian summer monsoon: impact of ocean mixed layer depth. *Journal of Climate*, **29 (21)**, 7889–7910.

Li, Y., W. Han, W. Wang, L. Zhang, and M. Ravichandran, 2018: The Indian Summer Monsoon Intraseasonal Oscillations in CFSv2 Forecasts: Biases and Importance of Improving AirSea

Interaction Processes. *J. Climate*, **31 (14)**, 5351–5370, doi:10.1175/JCLI-D-17-0623.1, URL https://journals.ametsoc.org/doi/full/10.1175/JCLI-D-17-0623.1.

MacKinnon, J. A., and Coauthors, 2016: A Tale of Two Spicy Seas. *Oceanography*, **29 (2)**, 50–61, URL https://www.jstor.org/stable/24862669.

McWilliams, J. C., and P. P. Sullivan, 2000: Vertical Mixing by Langmuir Circulations. *Spill Science & Technology Bulletin*, **6 (3)**, 225–237, doi:10.1016/S1353-2561(01)00041-X, URL http://www.sciencedirect.com/science/article/pii/S135325610100041X.

McWilliams, J. C., P. P. Sullivan, and C.-H. Moeng, 1997: Langmuir turbulence in the ocean. **334**, 1–30.

Mo, K. C., 2001: Adaptive Filtering and Prediction of Intraseasonal Oscillations. *Mon. Wea. Rev.*, **129 (4)**, 802–817, doi:10.1175/1520-0493(2001)129⟨0802:AFAPOI⟩2.0.CO;2, URL https://journals.ametsoc.org/doi/full/10.1175/1520-0493%282001%29129%3C0802%3AAFAPOI%3E2.0.CO%3B2.

Newman, M., and P. D. Sardeshmukh, 2017: Are we near the predictability limit of tropical indo-pacific sea surface temperatures? *Geophysical Research Letters*, **44 (16)**, 8520–8529.

Pattanaik, D. R., B. Mukhopadhyay, A. Kumar, and Coauthors, 2012: Monthly forecast of indian southwest monsoon rainfall based on nceps coupled forecast system. *Atmospheric and Climate Sciences*, **2 (04)**, 479.

Penland, C., and T. Magorian, 1993: Prediction of Nio 3 Sea Surface Temperatures Using Linear Inverse Modeling. *J. Climate*, **6 (6)**, 1067–1076, doi:10.1175/1520-0442(1993)006⟨1067:PONSST⟩2.0.CO;2, URL https://journals.ametsoc.org/doi/abs/10.1175/1520-0442(1993)006%3C1067:PONSST%3E2.0.CO%3B2.

Ramachandran, S., and Coauthors, 2018: Submesoscale Processes at Shallow Salinity Fronts in the Bay of Bengal: Observations during the Winter Monsoon. *Journal of Physical Oceanography*, **48 (3)**, 479–509, doi:10.1175/JPO-D-16-0283.1, URL http://journals.ametsoc.org/doi/10.1175/JPO-D-16-0283.1.

Samanta, D., S. N. Hameed, D. Jin, V. Thilakan, M. Ganai, S. A. Rao, and M. Deshpande, 2018: Impact of a Narrow Coastal Bay of Bengal Sea Surface Temperature Front on an Indian Summer Monsoon Simulation. *Scientific Reports*, **8 (1)**, 17 694, doi:10.1038/s41598-018-35735-3, URL https://www.nature.com/articles/s41598-018-35735-3.

Sarkar, S., H. Pham, S. Ramachandran, J. Nash, A. Tandon, J. Buckley, A. Lotliker, and M. Omand, 2016: The Interplay Between Submesoscale Instabilities and Turbulence in the Surface Layer of the Bay of Bengal. *Oceanography*, **29 (2)**, 146–157, doi:10.5670/oceanog.2016.47, URL https://tos.org/oceanography/article/the-interplay-between-submesoscale-instabilities-and-turbulence-in-the-surf.

Schmidtko, S., G. C. Johnson, and J. M. Lyman, 2013: Mimoc: A global monthly isopycnal upper-ocean climatology with mixed layers. *Journal of Geophysical Research: Oceans*, **118 (4)**, 1658–1672, doi:https://doi.org/10.1002/jgrc.20122, URL https://agupubs.onlinelibrary.wiley.com/doi/abs/10.1002/jgrc.20122, https://agupubs.onlinelibrary.wiley.com/doi/pdf/10.1002/jgrc.20122.

Sengupta, D., B. N. Goswami, and R. Senan, 2001: Coherent intraseasonal oscillations of ocean and atmosphere during the Asian Summer Monsoon. *Geophys. Res. Lett.*, **28 (21)**, 4127–4130, doi:10.1029/2001GL013587, URL http://onlinelibrary.wiley.com/doi/10.1029/2001GL013587/abstract.

Spiro Jaeger, G., and A. Mahadevan, 2018: Submesoscale-selective compensation of fronts in a salinity-stratified ocean. *Science Advances*, **4 (2)**, e1701 504, doi:10.1126/sciadv.1701504, URL http://advances.sciencemag.org/lookup/doi/10.1126/sciadv.1701504.

Suhas, E., J. M. Neena, and B. N. Goswami, 2013: An Indian monsoon intraseasonal oscillations (MISO) index for real time monitoring and forecast verification. *Clim Dyn*, **40 (11-12)**, 2605–2616, doi:10.1007/s00382-012-1462-5, URL https://link.springer.com/article/10.1007/s00382-012-1462-5.

Suzuki, N., and B. Fox-Kemper, 2016: Understanding stokes forces in the wave-averaged equations. *Journal of Geophysical Research: Oceans*, **121 (5)**, 3579–3596.

Thomson, R. E., and W. J. Emery, 2001: *Data Analysis Methods in Physical Oceanography*. 2nd ed., Elsevier Science, Amsterdam ; New York.

Van Roekel, L., B. Fox-Kemper, P. Sullivan, P. Hamlington, and S. Haney, 2012: The form and orientation of langmuir cells for misaligned winds and waves. *Journal of Geophysical Research: Oceans*, **117 (C5)**.

Weare, B. C., and J. S. Nasstrom, 1982: Examples of Extended Empirical Orthogonal Function Analyses. *Mon. Wea. Rev.*, **110 (6)**, 481–485, doi:10.1175/1520-0493(1982)110⟨0481:EOEEOF⟩2.0.CO;2, URL https://journals.ametsoc.org/doi/abs/10.1175/1520-0493(1982)110%3C0481:EOEEOF%3E2.0.CO%3B2.

Weiss, J. B., B. Fox-Kemper, D. Mandal, A. D. Nelson, and R. K. Zia, 2019: Nonequilibrium oscillations, probability angular momentum, and the climate system. *Journal of Statistical Physics*, 1–18.

Zhang, G. J., X. Song, and Y. Wang, 2019: The double itcz syndrome in gcms: A coupled feedback problem among convection, clouds, atmospheric and ocean circulations. *Atmospheric Research*, **229**, 255–268.

Zhang, L., W. Han, Y. Li, and E. D. Maloney, 2018: Role of North Indian Ocean AirSea Interaction in Summer Monsoon Intraseasonal Oscillation. *J. Climate*, **31 (19)**, 7885–7908, doi:10.1175/JCLI-D-17-0691.1, URL https://journals.ametsoc.org/doi/abs/10.1175/JCLI-D-17-0691.1.

LIST OF TABLES

TABLE 1. List of CESM case studies used in this study.

	KPP	Langmuir	Submesoscale
CTRL	x	x	x
noLT	x		x
noSM	x	x	
noLTSM	x		

LIST OF FIGURES

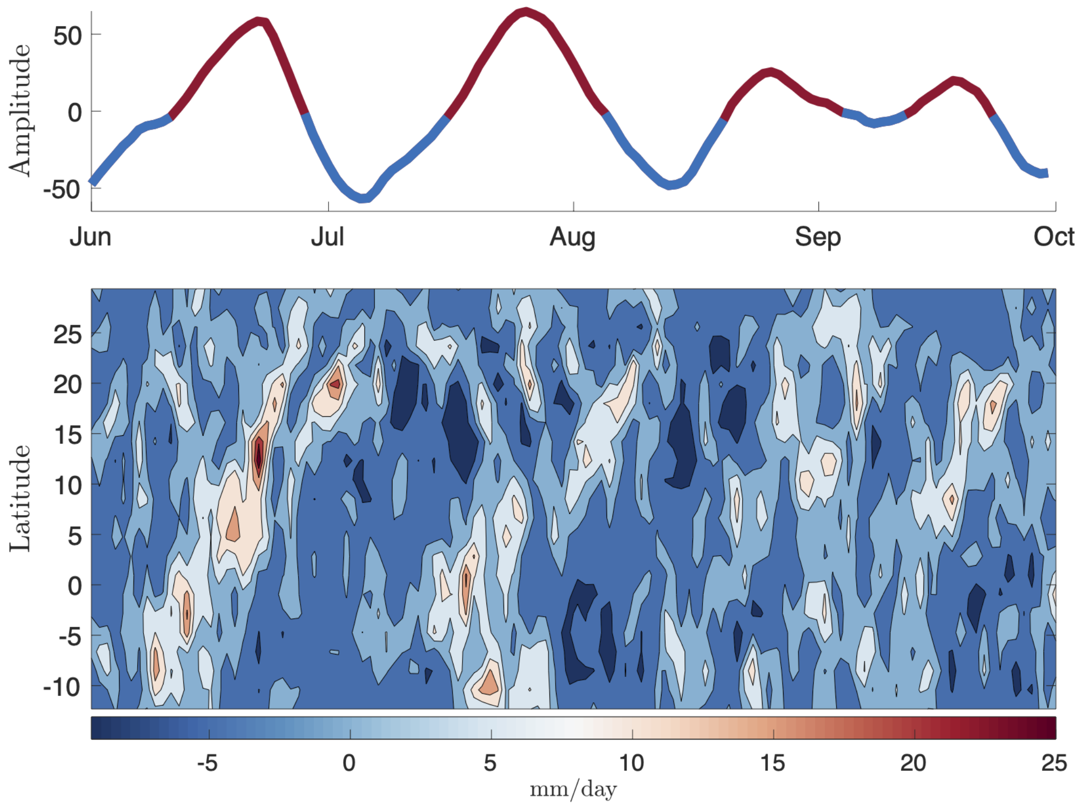

FIG. 1. Example of EEOF index method for Summer 2007 observed precipitation. EEOF1 index (top) is calculated from zonally averaged precipitation data (bottom) using method described in Section 2c. Diagonal areas of high precipitation correspond to northward-propagating rain bands, which in turn correspond to periods of positive EEOF1 (portions of the top plot in red).

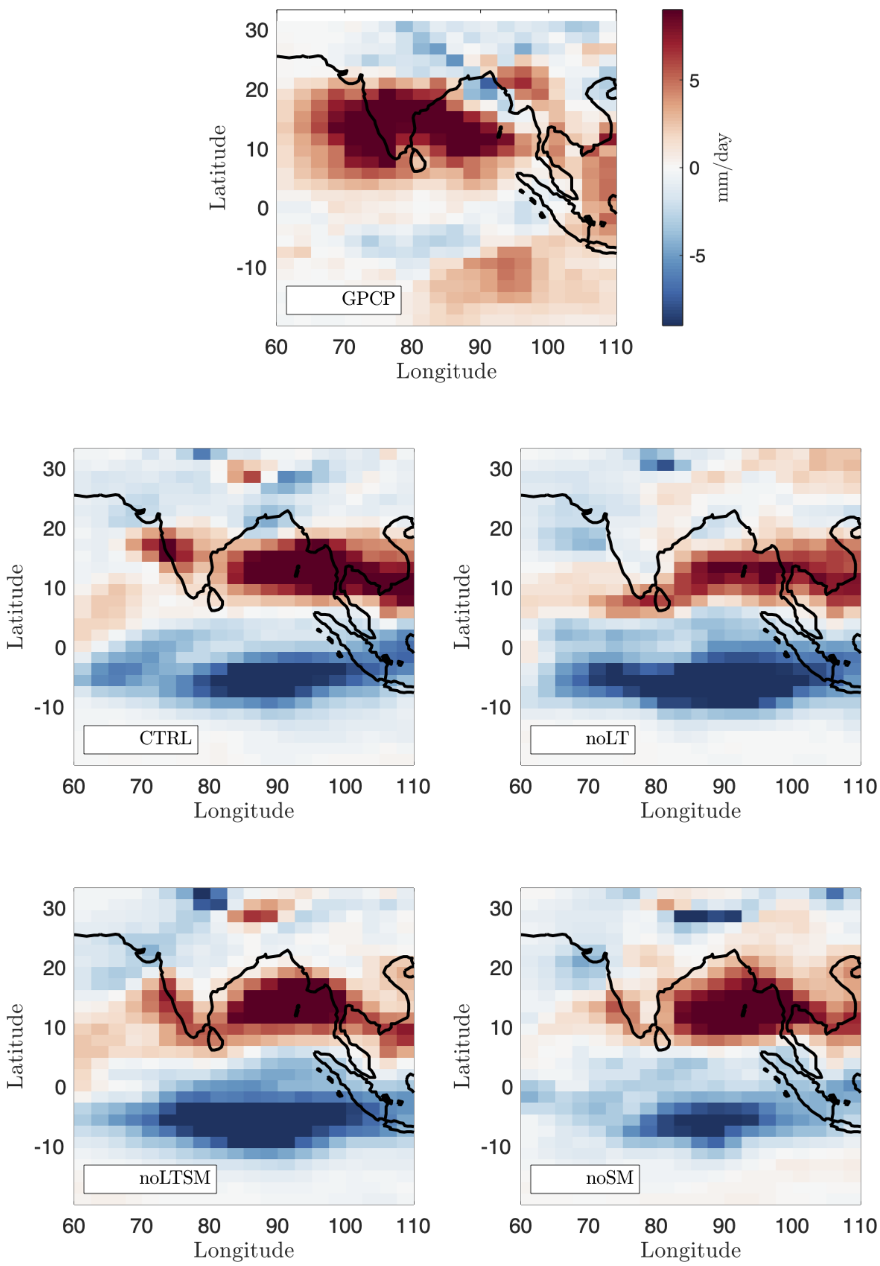

FIG. 2. Average difference in precipitation anomaly between positive and negative MISO1 phases. Maps show the difference between the average precipitation anomalies at all times for MISO1 $>$ 95th percentile and all times for MISO1 $<$ 5th percentile for the observations (top plot - GPCP) and for the cases (Table 1): CTRL = both Langmuir and submesoscale, noLT = submesoscale only, noSM = Langmuir only, noLTSM = neither parameterization, and GPCP = observations.

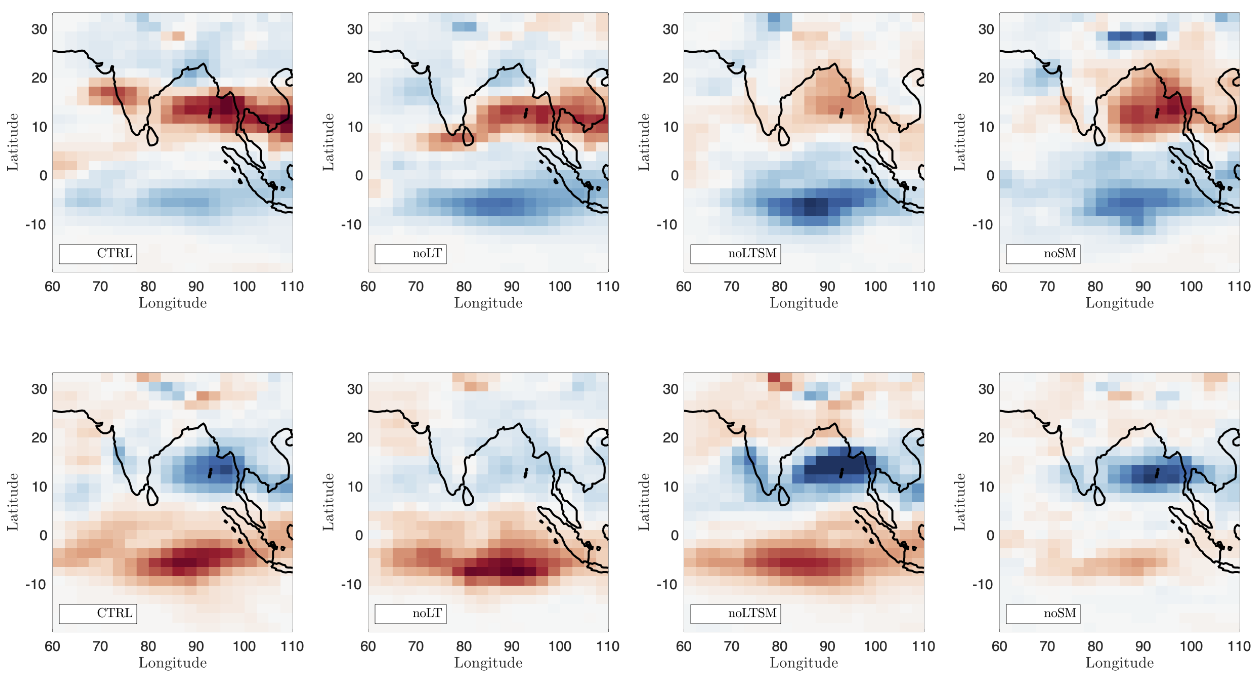

FIG. 3. Average positive and negative precipitation phases. Maps show the average precipitation anomalies at all times for MISO1 $>$ 95th percentile (top row) and all times for MISO1 $<$ 5th percentile (bottom row). Shown are the cases (Table 1): CTRL = both Langmuir and submesoscale, noLT = submesoscale only, noSM = Langmuir only, noLTSM = neither parameterization

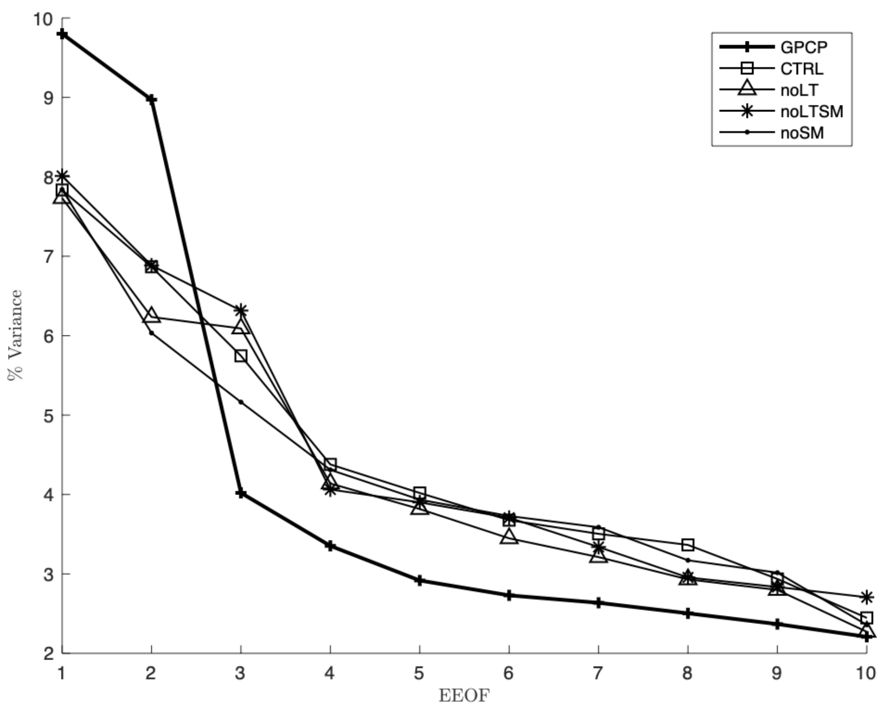

FIG. 4. Comparison of the relative importance of the first 10 EEOFs for GPCP observations and all model configurations. Method for calculating the percent of variance explained by each EEOF discussed in text. The first EEOF value corresponds to the percent variance represented by the MISO1 index. From Baylor: EEOF 1 and 2 of CESM represent a smaller fraction of the total variance when compared to EEOF 1 and 2 of the observations, but the precipitation variance in CESM is higher in $(\mathrm{mm/day})^2$, which may mean that the rainfall anomalies explained by EEOFs 1 and 2 of CESM matches that of the observations. Shown are the cases (Table 1): CTRL = both Langmuir and submesoscale, noLT = submesoscale only, noSM = Langmuir only, noLTSM = neither parameterization, and GPCP = observations.

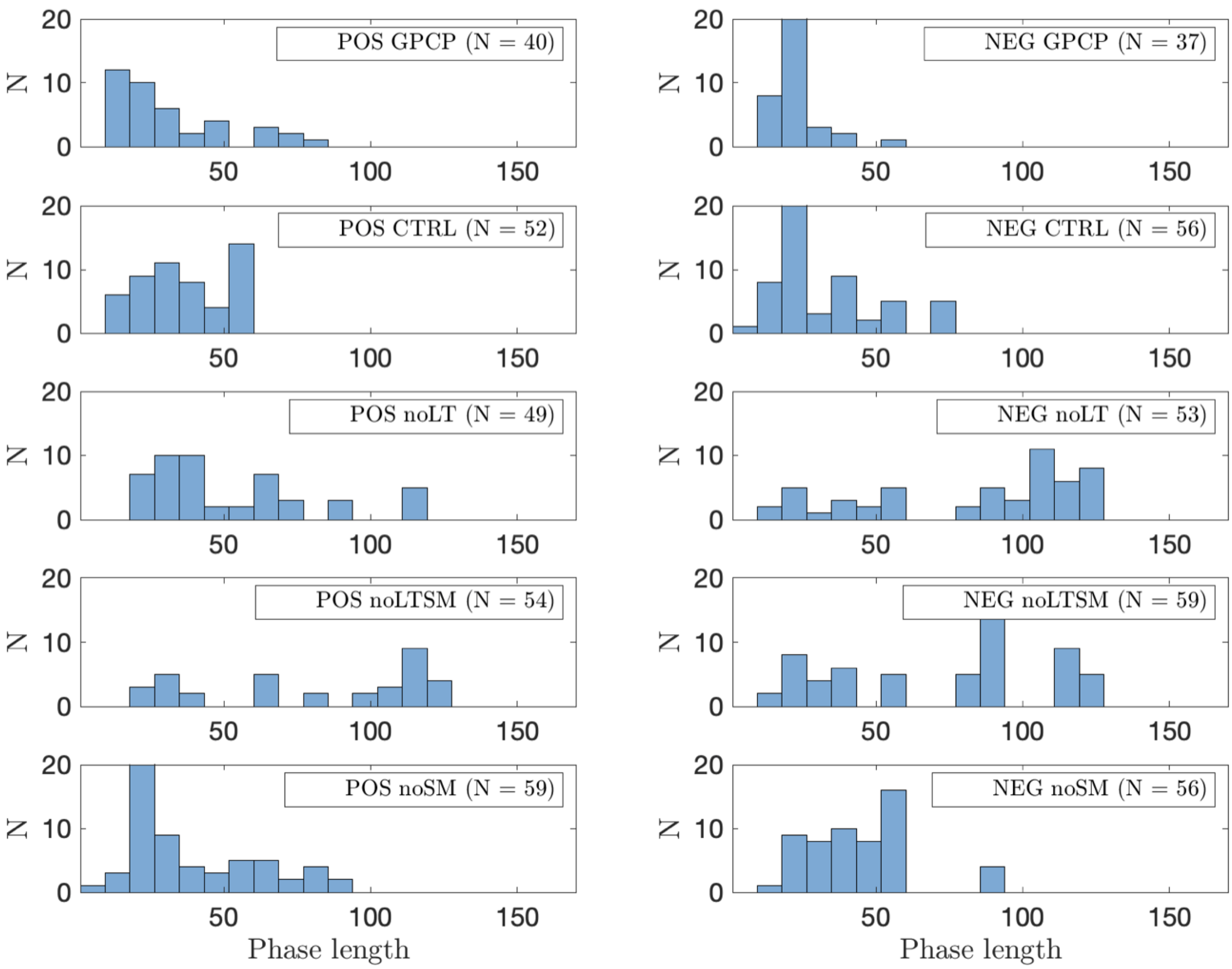

FIG. 5. Distribution of length in days of positive (left column) and negative (right column) phases of the MISO1 index for GPCP observations and all model configurations. Shown are the cases (Table 1): CTRL = both Langmuir and submesoscale, noLT = submesoscale only, noSM = Langmuir only, noLTSM = neither parameterization, and GPCP = observations.

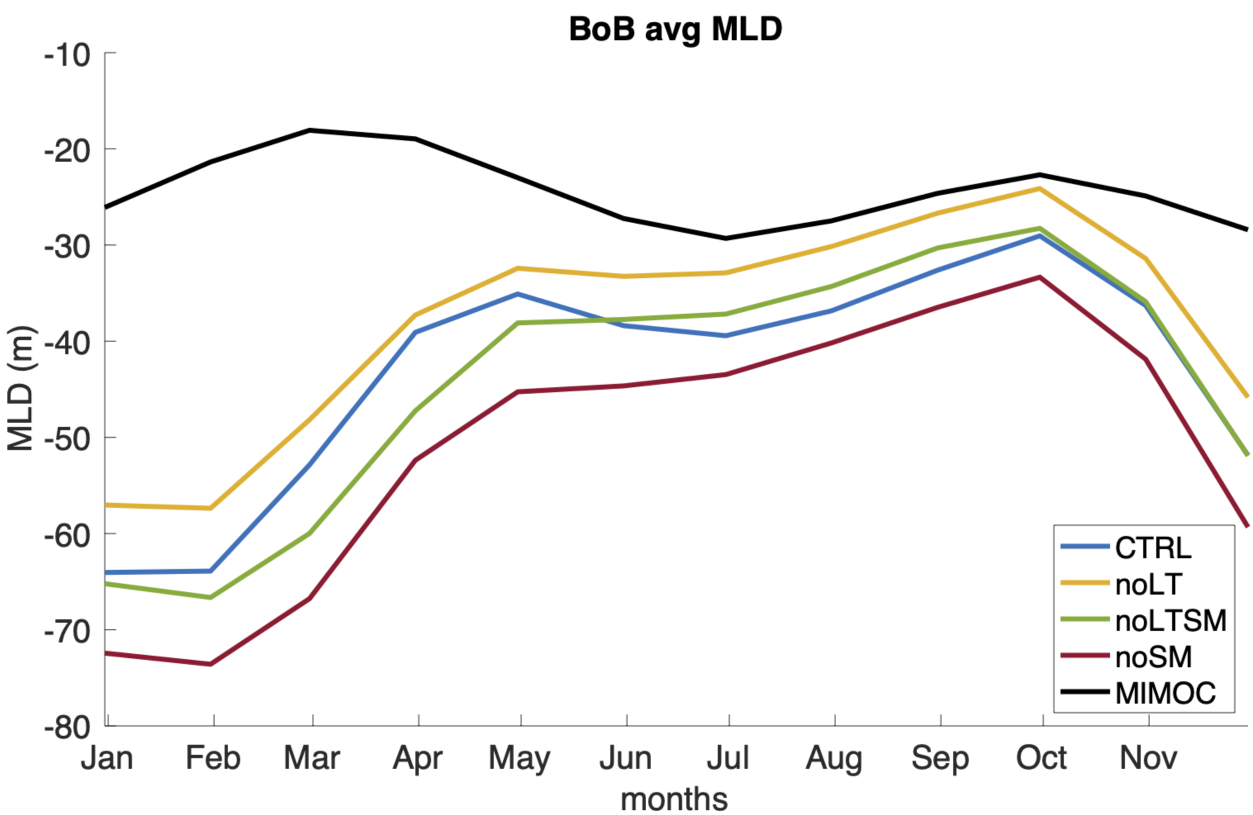

FIG. 6. Monthly climatology of spatially averaged mixed layer depth (MLD) in the Bay of Bengal from observations and for each model configuration. Observational data set from the Monthly Isopycnal & Mixed-layer Ocean Climatology (MIMOC) (Schmidtko et al. 2013)